

## A PULSAR WIND NEBULA MODEL APPLIED TO SHORT GRB 050724

WEI-LI LIN<sup>1,2</sup>, LING-JUN WANG<sup>3</sup>, ZI-GAO DAI<sup>1,2</sup>

<sup>1</sup>School of Astronomy and Space Science, Nanjing University, Nanjing 210093, China; dzg@nju.edu.cn

<sup>2</sup>Key Laboratory of Modern Astronomy and Astrophysics (Nanjing University), Ministry of Education, Nanjing 210093, China and

<sup>3</sup>Astroparticle Physics, Institute of High Energy Physics, Chinese Academy of Sciences, Beijing 100049, China

*Draft version March 12, 2018*

### ABSTRACT

A subset of short gamma-ray bursts (sGRBs) have been found to be characterized by near-infrared/optical bumps at  $\sim 1$  days, some of which exhibit almost concurrent X-ray flares. Although the near-infrared/optical bumps may be a signature of kilonovae, the X-ray flares are not consistent with kilonovae. It is widely believed that sGRBs are produced by the mergers of double compact objects, during which sub-relativistic ejecta are launched. In this paper we propose that the above optical/X-ray features are indicative of the formation of long-lived magnetars following the mergers of double neutron stars. Observations and theoretical works imply that the spin-down power of the magnetars is injected into the ejecta as ultra-relativistic electron-positron pairs, i.e. pulsar wind nebulae (PWNe). Here we suggest such a PWN model and find that the optical bump and X-ray flare observed in GRB 050724 can be well understood in this PWN model. We show that the optical bump and X-ray flare may have different origins. Our results strengthen the evidence for the formation of magnetars in double neutron star mergers and justify the validity of the PWN model.

*Subject headings:* gamma-ray burst: general – radiation mechanisms: non-thermal – stars: neutron

### 1. INTRODUCTION

Short gamma-ray bursts (sGRBs) have been widely believed to originate from the mergers of neutron star - neutron star (NS-NS) or neutron star - black hole (NS-BH) systems (Eichler et al. 1989; Narayan et al. 1992; Berger 2014). A recent gravitational-wave (GW) event (GW170817), has been identified as the signal from a binary neutron star inspiral (Abbott et al. 2017). The association of GW170817 with an sGRB (GRB 170817A) (Goldstein et al. 2017; Savchenko et al. 2017), provides a direct evidence for the binary NS coalescences as progenitors of at least part of sGRBs.<sup>1</sup>

The products of the NS-NS or NS-BH mergers are usually BHs. The outcome of NS-NS mergers could also be highly magnetized NSs (magnetars; Dai & Lu 1998a,b; Zhang & Mészáros 2001; Giacomazzo & Perna 2013; Giacomazzo et al. 2015). Direct identification of the merger product is at the reach of current advanced GW detectors. Although the mergers of NS-NS or NS-BH can be discerned by their different GW signals (Bartos et al. 2013), the combined detection of GW signals and their electromagnetic (EM) counterparts can improve our understanding of the physics of the merger process (Fernández & Metzger 2016), which can be a probe of the long-pursuing equation of state for supra-nuclear matter (Paschalidis 2017; Radice 2017).

The most energetic EM counterparts are sGRB prompt emission. If the merger product is a differentially rotating-supported supramassive magnetar that eventually collapses into a BH, the sGRB afterglow is characterized by shallow decay followed by steep decline (Rowlin-

son et al. 2010, 2013). However, sGRB and its immediate afterglow may not be the feasible candidate for the combined detection of a GW signal because of its low rate within the GW detection horizon due to the relativistic beaming effect.

Fortunately, there are a variety of almost isotropic EM counterparts that are bright enough to be easily detected. The NS magnetic interaction (Lai 2012; Piro 2012) with the companion NS or BH produces precursor emission in radio (Wang et al. 2016a) and X-ray (Palenzuela et al. 2013) bands. Sub-relativistic outflows would be launched by the mergers of NS-NS or NS-BH systems. The interaction of such outflows with surrounding interstellar medium (ISM) produces radio flares that are detectable for weeks (Nakar & Piran 2011).

If the merger product is a BH, the remnant could emerge as a kilonova heated by the radioactive  $r$ -process material (Li & Paczyński 1998; Metzger et al. 2010; Dietrich et al. 2017; Fernández et al. 2017; Metzger 2017). The evidence for such kilonovae boosted recently by the detection of near-infrared/optical bumps at  $\sim 1-10$  days following some sGRBs (Berger et al. 2013; Tanvir et al. 2013; Yang et al. 2015; Jin et al. 2016).<sup>2</sup>

If, on the other hand, the merger product is a magnetar, there could be very rich EM counterparts. The magnetic dissipation by a differentially rotating millisecond pulsar born after NS-NS merger could produce early-time multiple X-ray flares (Dai et al. 2006). The continuous energy injection by a stable post-merger magnetar will boost the luminosity of the radioactively powered kilonova to become a luminous mergernova (Yu et al. 2013) that lasts for  $\sim 10$  days in optical/ultraviolet bands. The interaction (forward shock) of the magnetar-aided ejecta with ISM will produce multi-band EM emission (Gao et

<sup>1</sup> Independent of a kilonova that can interpret the rapid evolution in ultraviolet/optical/near-infrared bands (e.g., Evans et al. 2017; Villar et al. 2017), both the X-ray and radio observations of GRB 170817A are consistent with either a mildly relativistic cocoon or an off-axis relativistic jet (e.g., Hallinan et al. 2017; Margutti et al. 2017; Troja et al. 2017; Xiao et al. 2017).

<sup>2</sup> The early X-ray light curve of GRB 130603B was attributed to a short-lived magnetar by Fan et al. (2013).

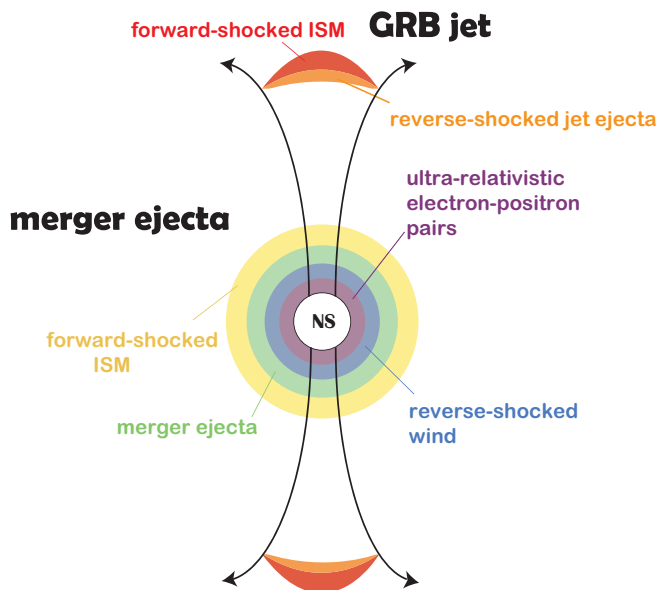


FIG. 1.— Schematic diagram of the evolution of an sGRB and a PWN after the formation of a post-merger millisecond magnetar.

al. 2013; Yu et al. 2013).

Some sGRBs (e.g., GRB 050724, GRB 061006, GRB 070714B and GRB 080503) show optical bumps a few days in length, a few of which (GRB 050724 and GRB 080503) were accompanied by almost concurrent X-ray flares. Different models were put forward to account for these features. For example, Panaitescu (2007) proposed that the X-ray flare in the afterglow light curve of GRB 050724 was caused by an energy injection. Gao et al. (2015, 2017) attributed the late optical re-brightenings to the mergernova emission. To account for their concurrent X-ray flares, Gao et al. (2015, 2017) proposed that the X-ray emission is a leakage of the spin-down luminosity of the magnetars.

An alternative scenario (Wang & Dai 2013; Wang et al. 2015, 2016b) about the multi-band emission of the magnetar-powered post-merger systems is based on the observations (Gaensler & Slane 2006; Hester 2008) and theories (Rees & Gunn 1974; Kennel & Coroniti 1984a,b; Begelman & Li 1992; Chen & Beloborodov 2017) of pulsar wind nebulae (PWNe), which are generated by the complex interactions between the magnetar wind, ejecta, and ambient ISM. The model, different from the above mergernova model (Yu et al. 2013; Gao et al. 2015), is built on the basis that the magnetar wind is Poynting flux dominated initially and then converted into energy flux of ultra-relativistic electron-positron pairs ( $e^+e^-$  pairs; Coroniti 1990; Michel 1994; Dai 2004; Yu & Dai 2007, see also Geng et al. 2016 for the applications to GRB jets).<sup>3</sup>

Here we follow the PWN model (Wang et al. 2015). In this model, the ejecta accelerated by the pressure of the magnetar wind sweeps up the ambient medium to form a forward shock. The interaction between the ejecta and magnetar wind forms a lepton-dominated reverse shock,

<sup>3</sup> The effect of wind magnetization is studied by Liu et al. (2016) based on the work of Zhang & Kobayashi (2005).

as schematized in Figure 1. In the original model (Wang et al. 2015) the energy loss due to the reverse-shock emission was ignored, as we always do in the modeling of GRB afterglow. However, because the reverse shock is lepton-dominated, the shock energy is carried mainly by leptons, whose energy loss will have a significant impact on the shock dynamics.

In this work, the energy loss due to the reverse-shock emission is considered. With such a revised PWN model, together with the GRB afterglow model, we interpret the X-ray flare at  $\sim 1$  day after the trigger of GRB 050724 as originating from the PWN reverse-shock emission, and the optical bump originating from the ejecta thermal emission. This paper is organized as follows. In Section 2, we introduce the GRB afterglow and PWN models used in this work. In Section 3, we show the fitting results to multi-band observations of GRB 050724. Finally, we discuss and conclude our findings in Section 4.

## 2. MODEL DESCRIPTION

### 2.1. GRB afterglow

The merger of NS-NS binary triggers the launch of a collimated relativistic jet. This jet gives rise to a forward shock that moves outward into the ISM and a reverse shock that backs into the unshocked ejecta (e.g., Sari & Piran 1995, 1999; Kobayashi 2000; Kobayashi & Sari 2000). Listed here are four regions of interest, namely, the unshocked ambient medium (region 1), forward-shocked medium (region 2), reverse-shocked ejecta (region 3) and unshocked ejecta (region 4). In a similar way as used by Huang et al. (2000) and Lan et al. (2016), the non-rest energy of this system can be expressed as

$$E_j = (\gamma_j^2 - 1)M_{sw,j}c^2 + (\gamma - 1)M_{3,j}c^2 + \gamma_j U'_{3,j} + (\gamma_{4,j} - 1)(M_{ej,j} - M_{3,j})c^2, \quad (1)$$

where  $\gamma_j$  is the bulk Lorentz factor of the jet,  $\gamma_{4,j}$  is the Lorentz factor of region 4,  $M_{sw,j}$  is the mass of swept-up ambient medium (with number density  $n$ ),  $M_{ej,j}$  is the mass of ejecta (i.e., initial mass of the jet),  $M_{3,j}$  is the mass of reverse-shocked ejecta, and  $U'_{3,j}$  is the internal energy of region 3 measured in the co-moving frame.

Energy conservation yields

$$\frac{d\gamma_j}{dt} = - \frac{\gamma_j \mathcal{D} \frac{dU'_{3,j}}{dt'} / c^2 + (\gamma_j^2 - 1) \frac{dM_{sw,j}}{dt} + (\gamma_j - \gamma_{4,j}) \frac{dM_{3,j}}{dt}}{U'_{3,j} / c^2 + 2\gamma_j M_{sw,j} + M_{3,j}}, \quad (2)$$

where the co-moving-frame time  $t'$  is equal to observer's time  $t$  multiplied by the Doppler factor  $\mathcal{D}$ .

Before the reverse shock crosses region 4, the evolution of  $U'_{3,j}$  depends mostly on the reverse shock process, (i.e.,  $dU'_{3,j} = (\gamma_{34,j} - 1)dM_{3,j}c^2$ , where  $\gamma_{34,j}$  is the Lorentz factor of the jet measured in the frame of region 4). However, after the cross time  $t_c$ , region 3 evolves in an adiabatic expansion, where we adopt (see also Equation (7) of Lan et al. 2016)

$$\frac{dU'_{3,j}}{dt'} = - \frac{1}{3} \frac{e'_{3,j}(t_c) V_{3,j}^{\prime \frac{4}{3}}(t_c)}{V_{3,j}^{\prime \frac{4}{3}}} \frac{dV'_{3,j}}{dt'}, \quad (3)$$

with  $V'_{3,j}$  and  $e'_{3,j}$  being the co-moving-frame volume and internal energy density of region 3, respectively.

The calculation of other relevant quantities is presented in Appendix A. In the context of GRB afterglow, we do not consider the effect of radiative loss on dynamics because the energy fraction of the shocked electrons is relatively low.

## 2.2. PWN powered by the magnetar wind

The coalescence of binary NSs ejects sub-relativistic and near-isotropic outflows with masses  $10^{-4} - 10^{-2} M_\odot$  (Rezzolla et al. 2010; Bauswein et al. 2013; Hotokezaka et al. 2013; Baiotti & Rezzolla 2017; Ciolfi et al. 2017). If the merger product is a stable magnetar, the Poynting flux in the immediate vicinity of the magnetar is converted to  $e^+e^-$  pairs that power the ejecta to form a PWN (Gaensler & Slane 2006; Aharonian et al. 2012). The merger ejecta are sandwiched between the ambient medium and magnetar wind and become a thin layer. The evolution of the PWN is shown in Figure 1. In this diagram, there are five regions, including the unshocked ambient medium (region 1), shocked medium (region 2), merger ejecta (ejecta region), shocked magnetar wind (region 3) and unshocked magnetar wind (region 4).

We investigate the dynamical evolution of the ejecta powered by a newborn millisecond magnetar wind (i.e., ultra-relativistic  $e^+e^-$  pairs). The spin-down luminosity carried by the wind is  $L_{\text{sd}} = L_0(1 + t/t_{\text{sd}})^{-2}$  with  $L_0 \approx 10^{47} B_{14}^2 R_6^6 P_{0,-3}^{-4}$  erg s $^{-1}$  and spin-down timescale  $t_{\text{sd}} \approx 2 \times 10^5 I_{45} B_{14}^{-2} P_{0,-3}^2 R_6^{-6}$  s, where the magnetar is characterized by the following parameters: the surface magnetic field strength  $B$ , initial spin period  $P_0$ , moment of inertia  $I$  and stellar radius  $R$ . Here we adopt the convention  $Q = 10^n Q_n$  in cgs units and set  $I_{45} = 1.5$  and  $R_6 = 1$ .

The total energy of this system with Lorentz factor  $\gamma$  can be written as

$$E = \gamma^2 M_{\text{sw}} c^2 + \gamma M_{\text{ej}} c^2 + \gamma M_3 c^2 + \gamma (U'_{\text{ej}} + U'_3). \quad (4)$$

Analogous to the notation in Section 2.1,  $\gamma_4$  is the Lorentz factor of the region 4,  $M_{\text{sw}}$  is the mass of forward-shocked ambient medium,  $M_{\text{ej}}$  is the mass of merger ejecta,  $M_3$  is the mass of reverse-shocked magnetar wind, and  $U'_{\text{ej}}$  and  $U'_3$  are the internal energy of corresponding regions in the co-moving frame. As seen in this expression, instead of considering the total energy evolution of region 3 (Wang et al. 2015), we list separately kinetic and internal energy of region 3.

In light of the energy conservation, we can obtain the dynamics as

$$\frac{d\gamma}{dt} = \frac{\left[ \frac{dE}{dt} - \gamma \mathcal{D} \left( \frac{dU'_{\text{ej}}}{dt'} + \frac{dU'_3}{dt'} \right) \right] / c^2 - \gamma^2 \frac{dM_{\text{sw}}}{dt} - \gamma \frac{dM_3}{dt}}{\left( U'_{\text{ej}} + U'_3 \right) / c^2 + 2\gamma M_{\text{sw}} + M_{\text{ej}} + M_3}. \quad (5)$$

The internal energy of region 3 evolves as

$$\frac{dU'_3}{dt'} = \frac{dU'_{3,\text{rs}}}{dt'} - L'_3 - p'_3 \frac{dV'_{3,\text{enc}}}{dt'}. \quad (6)$$

The internal energy increment  $dU'_{3,\text{rs}} = (\gamma_{34} - 1) dM_3 c^2$  corresponds to the instantaneously reverse-shocked  $e^+e^-$ . We demonstrate  $dU'_{3,\text{rs}}/dt' \sim L'_{\text{sd}} (= \mathcal{D}^2 L_{\text{sd}})$  for low bulk Lorentz factor in the Appendix B.

The radiation luminosity  $L'_3$  due to reverse-shock emission can be expressed as

$$L'_3 = \epsilon_{\text{r,rs}} \frac{dU'_{3,\text{rs}}}{dt'}, \quad (7)$$

where the radiative efficiency can be estimated by a function of the electron equipartition factor  $\epsilon_{\text{e,rs}}$ , and the co-moving-frame timescales of expansion and synchrotron cooling ( $t'_{\text{ex}}$  and  $t'_{\text{syn}}$ ; Dai et al. 1999; Huang et al. 2000), i.e.,

$$\epsilon_{\text{r,rs}} = \epsilon_{\text{e,rs}} \frac{t'^{-1}_{\text{syn}}}{t'^{-1}_{\text{syn}} + t'^{-1}_{\text{ex}}}. \quad (8)$$

Because the reverse-shocked  $e^+e^-$  pairs are in fast cooling regime, radiative efficiency is determined by  $\epsilon_{\text{e,rs}}$ . The high value,  $\epsilon_{\text{e,rs}} = 0.9$ , as adopted by Dai (2004), indicates the significant radiation loss of region 3, which is ignored in Wang et al. (2015). Consequently, reverse-shock emission comes from leptons that just get heated by reverse shock, rather than all shocked leptons in region 3.

As for the third term in Equation (6), the average pressure in region 3 is  $p'_3 = U'_3/(3V'_3)$  and the co-moving volume enclosed by region 3, different from the comoving volume of region 3 ( $V'_3$ ), increases at

$$\frac{dV'_{3,\text{enc}}}{dt} = 4\pi r^2 \beta c. \quad (9)$$

The evolution of the internal energy of ejecta is related to the absorbed fraction of radiation luminosity from region 3, (i.e.,  $(1 - e^{-\tau})L'_3$ ), the thermal energy loss is similar to Kasen & Bildsten (2010)

$$L'_{\text{th}} = \frac{U'_{\text{ej}} c}{\max(1, \tau) \Delta'_{\text{ej}}}, \quad (10)$$

and the radioactive power (Korobkin et al. 2012)

$$L'_{\text{ra}} = 4 \times 10^{49} M_{\text{ej},-2} \left( \frac{1}{2} - \frac{1}{\pi} \arctan \frac{t' - t'_0}{t'_\sigma} \right)^{1.3} \text{ erg s}^{-1}, \quad (11)$$

where  $t'_0 = 1.3$  s,  $t'_\sigma = 0.11$  s and  $\tau = \kappa(M_{\text{ej}}/V'_{\text{ej}}) \Delta'_{\text{ej}}$  with  $\kappa$  being the opacity. In other words, we have

$$\frac{dU'_{\text{ej}}}{dt'} = (1 - e^{-\tau}) L'_3 + L'_{\text{ra}} - L'_{\text{th}}. \quad (12)$$

The work that the ejecta does on region 2 is counteracted by that region 3 material does on ejecta, so the total effect of these two works is neglected here (see detailed discussion in Wang et al. 2015).

A combination of energy evolution in every region gives the energy variation of the whole system, i.e.,

$$\frac{dE}{dt} = L_{\text{sd}} + \mathcal{D}^2 (L'_{\text{ra}} - L'_{\text{th}} - L'_3 e^{-\tau}) + \frac{dM_{\text{sw}}}{dt} c^2. \quad (13)$$

Based on the above differential equation, we can obtain the dynamics of merger ejecta system. Figure 2 displays the dynamical evolution of our model with and without consideration of radiation loss of region 3. In this model, a reverse shock is generated when the ultra-relativistic pulsar wind catches up with the sub-relativistic ejecta. Most of the spin-down energy is at first transferred into

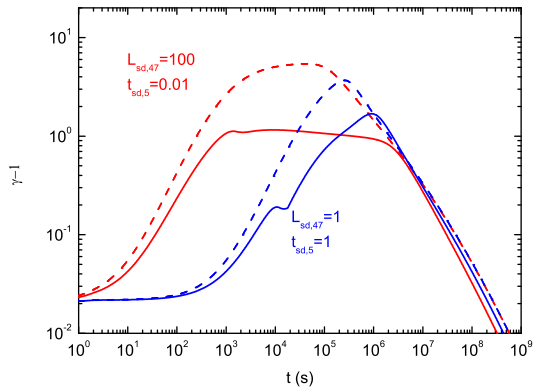


FIG. 2.— Dynamics derived from our PWN model (solid line) compared with results without consideration of radiation loss of region 3 (i.e., setting  $\epsilon_{r,rs} = 0$ ; dashed line). We also show the results of  $L_{sd} = 10^{47}$  erg s $^{-1}$  with  $t_{sd} = 10^5$  s (blue line) and  $L_{sd} = 10^{49}$  erg s $^{-1}$  with  $t_{sd} = 10^3$  s (red line), given that initial speed  $v_i = 0.2c$ ,  $M_{ej} = 10^{-3} M_{\odot}$ ,  $n_1 = 0.1$  cm $^{-3}$ ,  $\gamma_4 = 10^4$  and  $\kappa = 1$  cm $^2$  g $^{-1}$ .

the internal energy of reverse-shocked wind. Thus, at early times, its pressure is much higher than that of forward-shocked ISM and contributes to the acceleration of the whole system. However, because of radiation loss, the magnetar wind comprised of  $e^+e^-$  pairs cannot accelerate the total system efficiently. Moreover, due to the absorption and weak thermal emission of ejecta in the early time, a large amount of radiation energy is deposited into the internal energy of ejecta, which demands large energy budget for acceleration and in a way, slows down the speed-up process.

In addition, the ejecta system could be accelerated continuously even after  $t_{sd}$  (see the blue solid line in Figure 2 as an example) because several factors may contribute to the acceleration. The large amount of internal energy deposited in region 3 and ejecta could continuously accelerate the system. The radioactive decay of the material in ejecta could keep heating the ejecta. These factors may dominate over the decelerating effects such as the energy loss due to thermal emission of the ejecta for a while after  $t_{sd}$ . Figure 2 also indicates that for magnetars with the same rotational energy, the dynamics show strong dependence on the spin-down luminosity and spin-down timescale, which are determined by the spin period and magnetic field strength of the central magnetar. Thus, it can be concluded that the characteristics of central magnetar play an important role in the dynamics and consequently the emission of PWN components.

The shocked regions (regions 2 and 3) are characterized by synchrotron radiation, which is computed in a standard way (e.g., Wang et al. 2015). Compared with such synchrotron radiation, we consider thermal radiation in the ejecta, of which the flux at an observed frequency  $\nu$  can be expressed as

$$F_{\nu,th} = \frac{1}{\max(1, \tau_{\nu}) D_L^2} \frac{2\pi D^2 r^2}{h^3 c^2 \nu} \frac{\Delta'_{ej}}{r} \frac{(h\nu/D)^4}{\exp(h\nu/DkT') - 1}, \quad (14)$$

where  $\tau_{\nu}$  is the wavelength-dependent optical depth,  $D_L$  is the luminosity distance and  $T' = (e'_{ej}/a)^{1/4}$  denotes

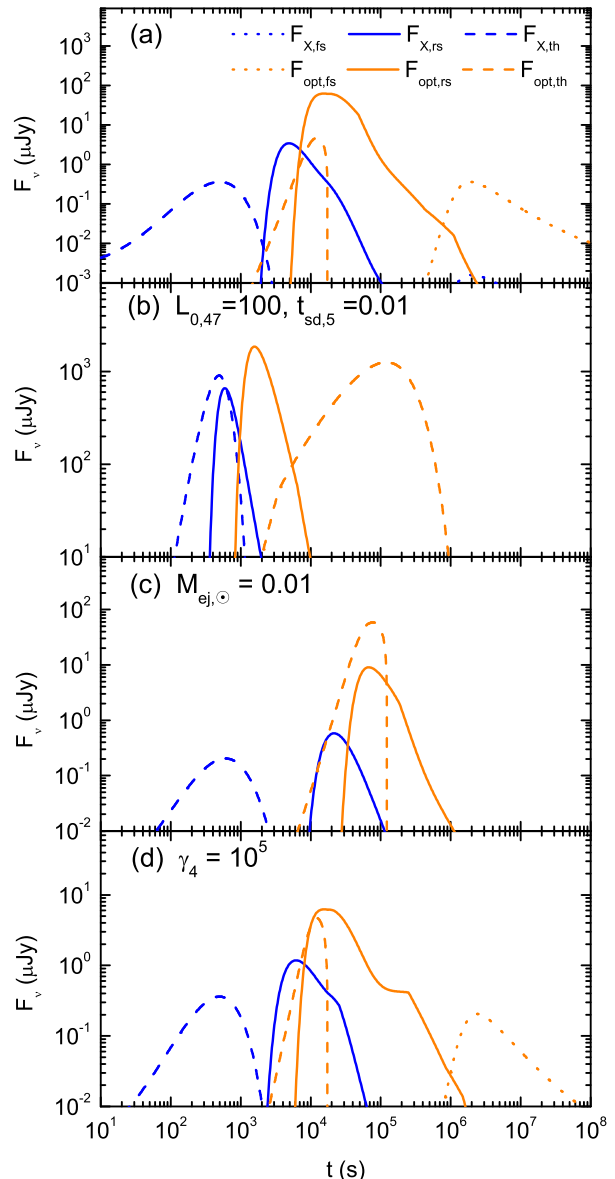


FIG. 3.— X-ray and optical light curves sensitive to the parameters in our PWN model. The dashed, dotted and solid lines correspond to the emission of thermal, forward shock and reverse shock in PWN system, respectively. Panel (a) results with parameters of redshift  $z = 0.2$ ,  $n_1 = 0.1$  cm $^{-3}$ ,  $L_{sd} = 10^{47}$  erg s $^{-1}$ ,  $t_{sd} = 10^5$  s,  $M_{ej} = 10^{-3} M_{\odot}$ ,  $v_i = 0.2c$ ,  $\gamma_4 = 10^4$ ,  $T'_i = 10^9$  K,  $\kappa = 1$  cm $^2$  g $^{-1}$ ,  $\kappa_X = 0.05$  cm $^2$  g $^{-1}$ ,  $\epsilon_{e,rs} = 0.9$ , electron and magnetic equipartition factors of forward shock ( $\epsilon_e = 0.1$ ,  $\epsilon_B = 0.01$ ). Other plots depict the light curves with one or two parameters altered. Panel (b)  $L_{sd} = 10^{49}$  erg s $^{-1}$ ,  $t_{sd} = 10^3$  s. Panel (c)  $M_{ej} = 10^{-2} M_{\odot}$ . Panel (d)  $\gamma_4 = 10^5$ .

the blackbody temperature. It should be noted that the pressure of ejecta  $p'_{ej} = e'_{ej}/3$  can be expressed as  $p'_{ej} = p'_3 + (1 - e^{-\tau})L'_3/(4\pi r^2 c)$ , where the second term is the radiation pressure corresponding to the radiation luminosity  $(1 - e^{-\tau})L'_3$ . Calculation of observed flux from both region 3 and ejecta should take into account the absorption and scattering effects of ejecta, so we denote the opacity  $\kappa$  for optical band and  $\kappa_X$  for X-ray band.

In the following, we study the emission features of the three regions and their dependence on some key param-

eters, based on comparison of the plots arranged in Figure 3.

We take the set of parameters used in Figure 3(a) as a control group and change one or two to see the difference. As X-ray light curves in Figure 3(a) show, the thermal emission peaks before the reverse-shock emission, while the forward shock emission dominates after  $\sim 10^6$  s. As for optical band, the reverse-shock emission dominates over the thermal emission, although they peak simultaneously. Figure 3(b) implies that faster energy injection leads to earlier, higher peaks of the reverse-shock emission and later, weaker peaks of the forward shock emission. As seen in Figure 3(c), the more massive the merger ejecta, the more important the thermal emission at optical band compared with the reverse-shock emission. According to Figure 3(d),  $\gamma_4$  only affects the components of reverse shock. In the case of higher  $\gamma_4$ , the reverse-shock emission reaches a lower peak value and then has a flatter decay.

Based on the multiwavelength behaviors of the thermal emission, we find that the X-ray peak always occurs much earlier than the optical peak. However, the X-ray peak of the reverse-shock emission is followed closely by the optical peak. In some cases, the thermal and reverse-shock emission at optical band peaks nearly simultaneously. Thus, this model can reproduce late bumps at different wavebands which occur almost at the same time.

### 3. APPLICATION

As can be seen in the fitting results of Gao et al. (2015, 2017), the afterglows of both GRB 080503 and GRB 050724 show the concurrence between optical/IR and X-ray bumps. For GRB 080503, however, since there are no confirmed redshift and fewer observational data, we choose GRB 050724 as the object for model fitting. Burst Alert Telescope on board the *Swift* satellite, at 12:34:09 UT on July 24th in 2005, triggered and detected GRB 050724 dominated by an initial hard peak lasting for 0.256 s (Covino et al. 2005; Krimm et al. 2005). Despite the duration  $T_{90} > 2$  s given by *Swift*, there are three pieces of evidence supporting that this burst can be classified as an sGRB (Barthelmy et al. 2005). Firstly, the duration derived from the 50keV-350keV data is consistent with the typical sGRB property. Secondly, the elliptical galaxy harboring GRB 050724 (at a redshift of 0.257; Berger et al. 2005) is a proper location for binary compact star mergers, which is the most promising progenitors of sGRBs. Lastly, the isotropic energy of the prompt emission is  $E_{\gamma, \text{iso}} \sim 10^{50}$  erg, which is 2  $\sim$  3 orders of magnitude lower than that of typical long GRBs.

The observational data of GRB 050724 in X-ray,  $R$  and radio (8.46 GHz) bands are collected from the literature (Berger et al. 2005; Burenin et al. 2005; Grupe et al. 2006; Panaitescu 2006; Malesani et al. 2007). The most prominent feature of the light curves of GRB 050724 is the optical bump and the bright X-ray flare occurred at approximately 1 day after the GRB trigger, as can be seen in Figure 4. Several models have been proposed to interpret this feature (Panaitescu 2007; Gao et al. 2015, 2017).

Here we propose that the optical bumps and X-ray flares at several days after the GRB trigger are related to PWN emission powered by a magnetar. The fitting results for GRB 050724 are shown in Figure 4 with adopted

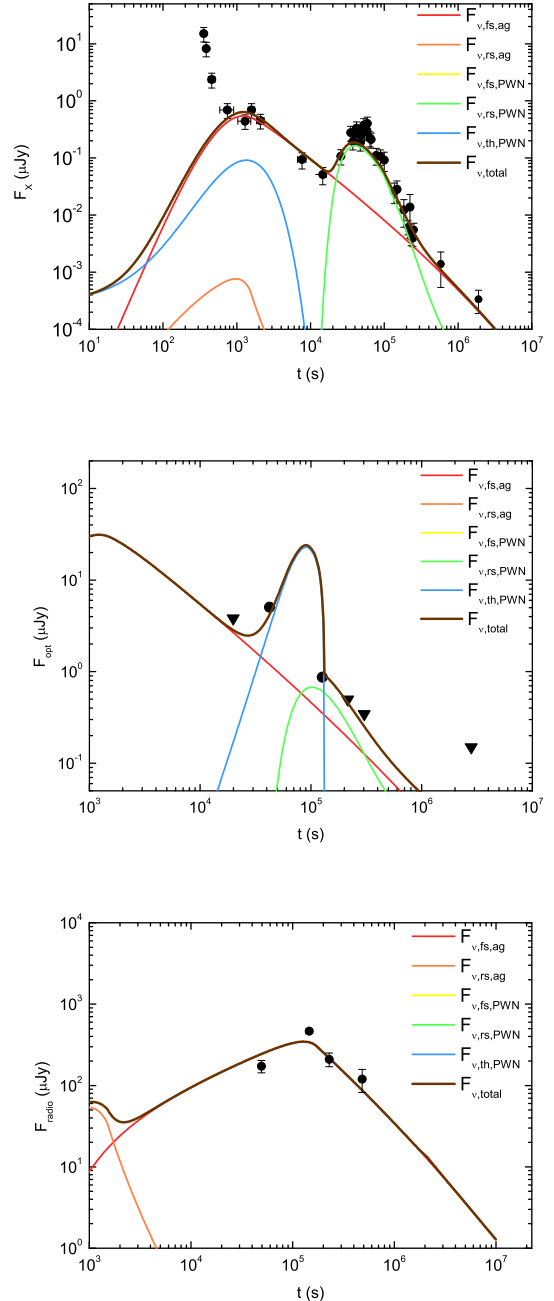


FIG. 4.— Fitting results to the broadband data of GRB 050724. The correction for Galactic or intrinsic extinction has not been applied to the optical data. Displayed are the contributions from the jet forward shock (red), jet reverse shock (orange) and merger ejecta system radiation comprised of the forward-shock emission (yellow), thermal emission (green) and reverse-shock emission (blue). The total flux is denoted as brown lines. It is shown that the emission from the reverse shock of the jet and the forward shock in the nebula is not notable.

parameters presented in Table 1.

Our fitting results are summarized in what follows. Our model suggests that the thermal radiation of the merger ejecta is responsible for the optical bump at  $\sim 1$  day, in agreement with the kilonova model. The reverse-shock emission from behind the merger ejecta proves to be capable of producing a late bright X-ray flare. Here

we suggest that the optical and X-ray re-brightenings both occurring at days after GRB trigger may not share the same origin, which is supported by the observations that optical bumps are not always accompanied by X-ray flares. The normal decay in the X-ray band after the flare, attributed here to the non jet-break before  $\sim 10^6$  s since burst, requires relatively large opening angle of the jet, which is consistent with the low degree of collimation suggested by [Grupe et al. \(2006\)](#).

In the following, we make a detailed analysis of the adopted parameters. The afterglow X-ray light curve with the decay slope  $\alpha_X = 0.98^{+0.11}_{-0.09}$  ([Grupe et al. 2006](#)), together with radio data, places a tight constraint on the electron spectral index  $p$ .<sup>4</sup> However, there are only loose constraints on other parameters associated with the afterglow component, i.e., the isotropic kinetic energy ( $E_{\text{iso},j}$ ), half opening angle ( $\theta_j$ ), Lorentz factor of region 4 ( $\gamma_{4,j}$ ), initial width of region 4 ( $\Delta_{4,i}$ ) and electron and magnetic equipartition factors ( $\epsilon_e, \epsilon_B$ ). Note that  $\epsilon_e$  and  $\epsilon_B$  are applied here in shock emission of all other cases except for the reverse-shocked magnetar wind which uses  $\epsilon_{e,rs}$  and  $\epsilon_{B,rs} = 1 - \epsilon_{e,rs}$ .

In the modeling of the magnetar-powered  $r$ -process ejecta, there is some uncertainty in the values of the ejecta opacities in the optical band  $\kappa$  and the X-ray band  $\kappa_X$  ([Wang et al. 2015](#)). During the time ( $\sim 1$  day) when the optical bump of GRB 050724 is prominent, the ejecta temperature is  $\gtrsim 10^5$  K. At such temperatures, the bound-bound opacity is negligible ([Kasen et al. 2013](#)). According to the analysis of [Wang et al. \(2015\)](#), the optical opacity of the ejecta is dominated by the bound-free opacity, which we estimate to be  $\kappa = 1 \text{ cm}^2 \text{ g}^{-1}$ . For opacity in X-ray band, we set  $\kappa_X = 0.1 \text{ cm}^2 \text{ g}^{-1}$ , which is close to the electron scattering opacity  $\kappa_{es} \approx 0.01 \text{ cm}^2 \text{ g}^{-1}$  ([Wang et al. 2015](#)). We choose such a value that is slightly larger than  $\kappa_{es}$  to account for the possible contribution from the bound-free transitions. We note that the resulting light curves are not sensitive to the initial temperature of the ejecta  $T_1'$ .

From the values of  $L_{sd}$  and  $t_{sd}$ , we can derive the properties of the central magnetar, i.e., surface magnetic field  $B = 2.7 \times 10^{14}$  G and initial spin period  $P_0 = 2.2$  ms, being consistent with the proposal of millisecond magnetars as likely products from the coalescence of binary NSs. Furthermore,  $t_{sd} = 2 \times 10^5$  s suggests a stable magnetar. The merger ejecta with mass  $M_{ej} = 10^{-2} M_\odot$  and initial speed of  $v_i = 0.2c$  meet the numerical simulations of NS-NS mergers, i.e.,  $M_{ej} \sim 10^{-4} - 10^{-2} M_\odot$  and  $v_i \sim 0.1 - 0.3c$  ([Hotokezaka et al. 2013](#)). The above results suggest that magnetar formation following NS-NS mergers is consistent with at least a subset of sGRBs.

## APPENDIX

### A. CALCULATION OF QUANTITIES IN GRB JETS

According to the mass conservation on both sides of the reverse-shock surface, the width of regions 3 and 4 increases by

$$d\Delta_{3,j} = \frac{(\beta_{4,j} - \beta_j)/\beta_{rs,j}}{\frac{\gamma_j n'_{3,j}}{\gamma_{4,j} n'_{4,j}} - 1} dr_j \quad (\text{A1})$$

<sup>4</sup> In principle the electron spectral indices of the forward- and reverse-shocked electrons can be different. In reality we found that

## 4. CONCLUSIONS

Several sGRBs are found to have prominent features of near-infrared/optical re-brightenings and X-ray flares at days after GRB triggers. These features are not expected in the standard afterglow model and are therefore a direct reflection of the continuous activity of the central engine.

In this paper we propose that these deviations from the standard afterglow model can be interpreted by the formation of stable magnetars following the mergers of double NSs. The rapidly-spinning magnetar blows up a nebula, as schematized in [Figure 1](#). In describing the PWN model modified from [Wang et al. \(2015\)](#), we stress the dynamic effect of significant radiation energy that is emitted by reverse-shocked  $e^+e^-$  pairs and strongly absorbed by the ejecta in the early time. The radiation energy loss or transfer weakens substantially the acceleration by the magnetar wind.

Based on the fitting results of the multi-band data of GRB 050724, we make main conclusions as follows. Firstly, a good fit to sGRB observations with the PWN model supports the formation of long-lived magnetars after NS-NS mergers. Secondly, late optical bumps are attributed to thermal radiation from merger ejecta which are heated by both the  $r$ -process material and reverse-shock radiation at early times. Thirdly, different from the origin of optical bumps, X-ray flares occurring at  $\sim 1$  day are likely to result from the synchrotron emission of reverse-shocked  $e^+e^-$  wind. Finally, due to the notable properties of nebula emission, we suggest that PWN could be an efficient probe for the NS-NS mergers and newborn millisecond magnetars.

The breakthrough detection of GW 170817 accompanied by rich electromagnetic counterparts including sGRB 170817A boosts the researches relevant to sGRBs and marks the beginning of a new era of multi-messenger astronomy. Future combined detections of NS-NS coalescences with total mass consistent with stable NSs and electromagnetic counterparts with PWN characteristics would further provide strong evidence for the PWN model presented in this paper.

We thank Fang-Kun Peng for his helpful discussion about the *Swift* data. This work was supported by the National Basic Research Program (“973” program) of China (grant No. 2014CB845800), the National Natural Science Foundation of China (grant No. 11573014) and the National Key R&D Program of China (grant no. 2017YFA0402600). L.J.W. was also supported by the National Program on Key Research and Development Project of China (Grant No. 2016YFA0400801).

the difference of adopting different values for these two parameters is small when fitting the observational data.

TABLE 1  
ADOPTED PARAMETERS FOR FITTING THE BROADBAND OBSERVATIONS OF GRB 050724.

Jet parameters							
$E_{\text{iso},j}$ (erg)	$\theta_j$ (rad)	$\gamma_{4,j}$	$\Delta_{4,i}$ (cm)				
$5 \times 10^{51}$	0.4	80	$10^{12}$				
PWN parameters							
$L_{\text{sd}}$ (erg s $^{-1}$ )	$t_{\text{sd}}$ (s)	$M_{\text{ej}}$ ( $M_{\odot}$ )	$v_i/c$	$\gamma_4$	$T'_i$ (K)	$\kappa$ (cm $^2$ g $^{-1}$ )	$\kappa_X$ (cm $^2$ g $^{-1}$ )
$3 \times 10^{46}$	$2 \times 10^5$	$10^{-2}$	0.2	$10^5$	$10^9$	1	0.1
Other parameters							
$n_1$ (cm $^{-3}$ )	$p$	$\epsilon_e$	$\epsilon_B$	$\epsilon_{e,\text{rs}}$			
0.0005	2.3	0.1	0.01	0.9			

$$d\Delta_{4,j} = -\frac{\gamma_j n'_{3,j}}{\gamma_{4,j} n'_{4,j}} d\Delta_{3,j}, \quad (\text{A2})$$

where  $\beta_{\text{fs},j} = \beta_j / (1 - 1/(4\gamma_j + 3)/\gamma_j)$  is the forward shock velocity in units of  $c$  and the number density ratio of region 3 and 4,  $n'_{3,j}/n'_{4,j} = 4\gamma_{34,j} + 3$  satisfies the shock jump conditions (Blandford & McKee 1976).

The other quantities about GRB jets evolve as

$$\frac{dr_j}{dt} = \frac{\beta_{\text{fs},j} c}{1 - \beta_{\text{fs},j}}, \quad (\text{A3})$$

$$\frac{d\theta_j}{dr_j} = c_s \mathcal{D} / r_j, \quad (\text{A4})$$

$$\frac{dM_{\text{sw},j}}{dr_j} = 4\pi(1 - \cos\theta_j)r_j^2 n m_p, \quad (\text{A5})$$

$$\frac{dM_{3,j}}{dr_j} = 4\pi(1 - \cos\theta_j)r_j^2 n'_3 m_p \gamma_j \frac{d\Delta_{3,j}}{dr_j}, \quad (\text{A6})$$

$$n'_{4,j} = \frac{M_{\text{ej},j}}{4\pi(1 - \cos\theta_j)r_{\text{ej}}^2 \gamma_4 \Delta_4 m_p}, \quad (\text{A7})$$

where  $r_j$  is the radius,  $\theta_j$  is the half opening angle of jets and  $n'_{4,j}$  is the comoving-frame number density of particles in region 4. Note that the sound speed  $c_s$  is calculated according to Equation (10) of Huang et al. (2000), which is applicable for both relativistic and non-relativistic scenarios.

#### B. THE INTERNAL ENERGY GAINED BY THE REVERSE SHOCK IN THE PWN

When typical parameters for PWNe are adopted, i.e.,  $\gamma_4 = 10^4$  and  $\beta \sim 0.1$ , we have the width of region 3  $d\Delta_3 \sim dr$ , leading to the conclusion that the reverse-shock surface stands near the central magnetar. So we can obtain  $dM_3/dt = L_{\text{sd}}/(\gamma_4 c^2)$  and then derive

$$\frac{dU'_{3,\text{rs}}}{dt'} = \frac{\gamma_{34} - 1}{\gamma_4} \mathcal{D} L'_{\text{sd}}. \quad (\text{B1})$$

By defining  $\eta \equiv \frac{dU'_{3,\text{rs}}/dt'}{L'_{\text{sd}}} = \frac{\gamma_{34} - 1}{\gamma_4} \mathcal{D}$ , the relation between  $\eta$  and  $\gamma - 1$  is shown in Figure 5, which suggests  $\frac{dU'_{3,\text{rs}}}{dt'} \sim L'_{\text{sd}}$ .

#### REFERENCES

- Abbott, B. P., Abbott, R., Abbott, T. D., et al. 2017, Physical Review Letters, 119, 161101
- Aharonian, F. A., Bogovalov, S. V., & Khangulyan, D. 2012, Natur, 482, 507
- Baiotti, L., & Rezzolla, L. 2017, RPPH, 80, 096901
- Barthelmy, S. D., Chincarini, G., Burrows, D. N., et al. 2005, Nature, 438, 994
- Bartos, I., Brady, P., & Márka, S. 2013, CQGra, 30, 123001
- Bauswein, A., Goriely, S., & Janka, H. T. 2013, ApJ, 773, 78
- Begelman, M. C., & Li, Z. Y. 1992, ApJ, 397, 187
- Berger, E. 2014, ARA&A, 52, 43
- Berger, E., Fong, W., & Chornock, R. 2013, ApJ, 774, L23
- Berger, E., Price, P. A., Cenko, S. B., et al. 2005, Nature, 438, 988
- Blandford, R. D., & McKee, C. F. 1976, Physics of Fluids, 19, 1130
- Burenin, R., Pavlinsky, M., Sunyaev, R., et al. 2005, GRB Coordinates Network, 3671, 1
- Chen, A. Y., Beloborodov, A. M. 2017, ApJ, 844, 133
- Ciolfi, R., Kastaun, W., Giacomazzo, B., et al. 2017, PhRvD, 95, 063016
- Coroniti, F. V. 1990, ApJ, 349, 538
- Covino, S., Antonelli, L. A., Romano, P., et al. 2005, GRB Coordinates Network, 3665, 1
- Dai, Z. G. 2004, ApJ, 606, 1000
- Dai, Z. G., & Lu, T. 1998a, A&A, 333, L87
- Dai, Z. G., & Lu, T. 1998b, PhRvL, 81, 4301
- Dai, Z. G., Huang, Y. F., & Lu, T. 1999, ApJ, 520, 634

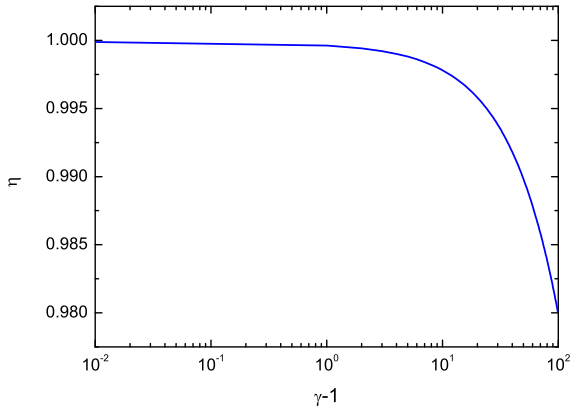


FIG. 5.—  $\eta$  as a function of  $\gamma - 1$ .

- Dai, Z. G., Wang, X. Y., Wu, X. F., & Zhang, B. 2006, *Science*, 311, 1127
- Dietrich, T., Ujevic, M., Tichy, W., et al. 2017, *PhRvD*, 95, 024029
- Eichler, D., Livio, M., Piran, T., & Schramm, D. N. 1989, *Nature*, 340, 126
- Evans, P. A., Cenko, S. B., Kennea, J. A., et al. 2017, *Sci*, 358, 1565
- Fan, Y.-Z., Yu, Y.-W., Xu, D., et al. 2013, *ApJ*, 779, L25
- Fernández, R., Foucart, F., Kasen, D., et al. 2017, *CQGra*, 34, 154001
- Fernández, R., & Metzger, B. D. 2016, *ARNPS*, 66, 23
- Gaensler, B. M., & Slane, P. O. 2006, *ARA&A*, 44, 17
- Gao, H., Ding, X., Wu, X.-F., Dai, Z.-G., & Zhang, B. 2015, *ApJ*, 807, 163
- Gao, H., Ding, X., Wu, X.-F., Zhang, B., & Dai, Z.-G. 2013, *ApJ*, 771, 86
- Gao, H., Zhang, B., Lü, H.-J., & Li, Y. 2017, *ApJ*, 837, 50
- Geng, J. J., Wu, X. F., Huang, Y. F., Li, L., & Dai, Z. G. 2016, *ApJ*, 825, 107
- Giacomazzo, B., & Perna, R. 2013, *ApJL*, 771, L26
- Giacomazzo, B., Zrake, J., Duffell, P. C., et al. 2015, *ApJ*, 809, 39
- Goldstein, A., Veres, P., Burns, E., et al. 2017, *ApJ*, 848, L14
- Grupe, D., Burrows, D. N., Patel, S. K., et al. 2006, *ApJ*, 653, 462
- Hallinan, G., Corsi, A., Mooley, K. P., et al. 2017, *Sci*, 358, 1579
- Hester, J. J. 2008, *ARA&A*, 46, 127
- Hotokezaka, K., Kiuchi, K., Kyutoku, K., et al. 2013, *Phys. Rev. D*, 87, 024001
- Huang, Y. F., Gou, L. J., Dai, Z. G., & Lu, T. 2000, *ApJ*, 543, 90
- Jin, Z.-P., Hotokezaka, K., Li, X., et al. 2016, *Nature Communications*, 7, 12898
- Kasen, D., Badnell, N. R., & Barnes, J. 2013, *ApJ*, 774, 25
- Kasen, D., & Bildsten, L. 2010, *ApJ*, 717, 245
- Kennel, C. F., & Coroniti, F. V. 1984a, *ApJ*, 283, 694
- Kennel, C. F., & Coroniti, F. V. 1984b, *ApJ*, 283, 710
- Kobayashi, S. 2000, *ApJ*, 545, 807
- Kobayashi, S., & Sari, R. 2000, *ApJ*, 542, 819
- Korobkin, O., Rosswog, S., Arcones, A., & Winteler, C. 2012, *MNRAS*, 426, 1940
- Krimm, H., Barbier, L., Barthelmy, S., et al. 2005, *GRB Coordinates Network*, 3667, 1
- Lai, D. 2012, *ApJ*, 757, L3
- Lan, M.-X., Wu, X.-F., & Dai, Z.-G. 2016, *ApJ*, 816, 73
- Li, L.-X., & Paczyński, B. 1998, *ApJ*, 507, L59
- Liu, L. D., Wang, L. J., & Dai, Z. G. 2016, *A&A*, 592, A92
- Margutti, R., Berger, E., Fong, W., et al. 2017, *ApJ*, 848, L20
- Malesani, D., Covino, S., D'Avanzo, P., et al. 2007, *A&A*, 473, 77
- Metzger, B. D. 2017, *LRR*, 20, 3
- Metzger, B. D., Martínez-Pinedo, G., Darbha, S., et al. 2010, *MNRAS*, 406, 2650
- Michel, F. C. 1994, *ApJ*, 431, 397
- Nakar, E., & Piran, T. 2011, *Nature*, 478, 82
- Narayan, R., Paczyński, B., & Piran, T. 1992, *ApJ*, 395, L83
- Palenzuela, C., Lehner, L., Ponce, M., et al. 2013, *PhRvL*, 111, 061105
- Panaitescu, A. 2006, *MNRAS*, 367, L42
- Panaitescu, A. 2007, *MNRAS*, 379, 331
- Paschalidis, V. 2017, *CQGra*, 34, 084002
- Piro, A. L. 2012, *ApJ*, 755, 80
- Radice, D. 2017, *ApJL*, 838, L2
- Rees, M. J., & Gunn, J. E. 1974, *MNRAS*, 167, 1
- Rezzolla, L., Baiotti, L., Giacomazzo, B., et al. 2010, *CQGra*, 27, 114105
- Rowlinson, A., O'Brien, P. T., Metzger, B. D., et al. 2013, *MNRAS*, 430, 1061
- Rowlinson, A., O'Brien, P. T., Tanvir, N. R., et al. 2010, *MNRAS*, 409, 531
- Sari, R., & Piran, T. 1995, *ApJ*, 455, L143
- Sari, R., & Piran, T. 1999, *ApJ*, 517, L109
- Savchenko, V., Ferrigno, C., Kuulkers, E., et al. 2017, *ApJ*, 848, L15
- Tanvir, N. R., Levan, A. J., Fruchter, A. S., et al. 2013, *Nature*, 500, 547
- Troja, E., Piro, L., van Eerten, H., et al. 2017, *Nature*, 551, 71
- Villar, V. A., Guillochon, J., Berger, E., et al. 2017, *ApJ*, 851, L21
- Wang, J. S., Yang, Y. P., Wu, X. F., Dai, Z. G., & Wang, F. Y. 2016a, *ApJ*, 822, L7
- Wang, L. J., & Dai, Z. G. 2013, *ApJ*, 774, L33
- Wang, L. J., Dai, Z. G., Liu, L. D., & Wu, X. F. 2016b, *ApJ*, 823, 15
- Wang, L. J., Dai, Z. G., & Yu, Y. W. 2015, *ApJ*, 800, 79
- Xiao, D., Liu, L.-D., Dai, Z.-G., & Wu, X.-F. 2017, *ApJ*, 850, L41
- Yang, B., Jin, Z.-P., Li, X., et al. 2015, *Nature Communications*, 6, 7323
- Yu, Y. W., & Dai, Z. G. 2007, *A&A*, 470, 119
- Yu, Y. W., Zhang, B., & Gao, H. 2013, *ApJ*, 776, L40
- Zhang, B., & Kobayashi, S. 2005, *ApJ*, 628, 315
- Zhang, B., & Mészáros, P. 2001, *ApJ*, 552, L35